Birefringent metamaterial nanocuboids with tailored optical constants for force and torque transduction

Ying Tang, Seungkyu Ha, Thomas Begou, Julien Lumeau, H Paul Urbach, Nynke H Dekker, Aurèle J L Adam

ACSNANO

www.acsnano.org

ARTICLE

Versatile Multilayer Metamaterial Nanoparticles with Tailored Optical Constants for Force and Torque Transduction

Ying Tang,[§] Seungkyu Ha,[§] Thomas Begou, Julien Lumeau, H. Paul Urbach, Nynke H. Dekker,* and Aurèle J. L. Adam*

Cite This: *ACS Nano* 2020, 14, 14895−14906

Read Online

ACCESS | Metrics & More | Article Recommendations | Supporting Information

ABSTRACT: The ability to apply force and torque directly to micro- and nanoscale particles in optical traps has a wide range of applications. While full control of both force and torque in three dimensions has been realized using top-down fabrication of rod-shaped particles composed of birefringent crystalline materials, widespread usage of such particles is limited as the optical constants of the predominant birefringent materials (quartz SiO_2 and rutile TiO_2) preclude coverage of the full application space of optical trapping. Here, we show that multilayer metamaterial nanoparticles provide access to a wide range of optical constants that can be specifically tuned for each application. Selecting the material pair Nb_2O_5/SiO_2 from the library of amorphous dielectrics as our metamaterial, we show that its refractive index and birefringence can be designed by adapting the ratio of layer thicknesses. Using a robust top-down fabrication process, we show that uniformly sized, free-floating Nb_2O_5/SiO_2 particles with high birefringence at moderate refractive index are obtained at high yield. Using an optical torque wrench, we show that these particles function as joint force and torque transducers while maintaining excellent stability in aqueous solutions and can be controllably optimized for particular physical characteristics such as maximal torque transfer or rapid response time. We expect that such customizable birefringent metamaterial nanoparticles whose properties surpass those of conventional crystalline particles will provide a means to unleash the full potential of optical trapping applications.

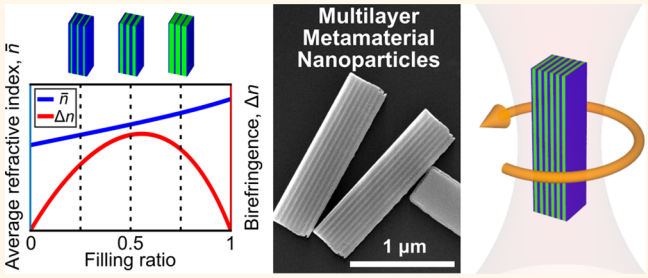

KEYWORDS: *metamaterials, dielectric multilayers, nanoparticles, optical trapping, force spectroscopy, torque spectroscopy*

The development of optical trapping has led to numerous micro- and nanoscale applications over the past decades.[1−3] The ability to perform contact-free optical manipulation and accurate detection of linear and angular motion has enabled technologies such as force and torque spectroscopy of single biomolecules,[4−7] quantum optomechanics,[8,9] colloidal self-assembly,[10] and optically driven nanomachines.[11] For such applications, dielectric materials, *e.g.*, silica and polystyrene (PS), have been popular choices as force transducers.[4] For the combined manipulation of force and torque, optically birefringent dielectric probes have proven their unique advantages over metallic probes,[12,13] enabling reduced scattering, less heating, straightforward torque detection *via* direct measurement of spin angular momentum transfer, and fully confined rotational degrees of freedom.[6] Various uniaxial birefringent crystals (Figure 1a) have been successfully applied as optical force and torque transducers, including quartz SiO_2,[14−18] calcite $CaCO_3$,[19] vaterite $CaCO_3$,[8,20] liquid crystal RM257,[21] and rutile TiO_2.[7,22,23]

Nonetheless, all these dielectrics come with particular limitations. Silica and PS are commercially available as highly uniform and chemically stable microspheres with a wide range of diameters and surface chemistries. However, they are not suitable as spin angular momentum-based torque transducers due to their absence of optical birefringence. Another chemically stable material, quartz SiO_2, is optically birefringent and thus permits straightforward transfer and detection of torque. Moreover, the ability to produce rod-shaped birefringent quartz SiO_2 particles using top-down fabrication[14−18] is highly beneficial for torsional control, as such particle geometry allows for fully constrained rotational

Received: May 20, 2020
Accepted: October 23, 2020
Published: November 10, 2020

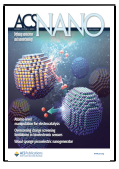

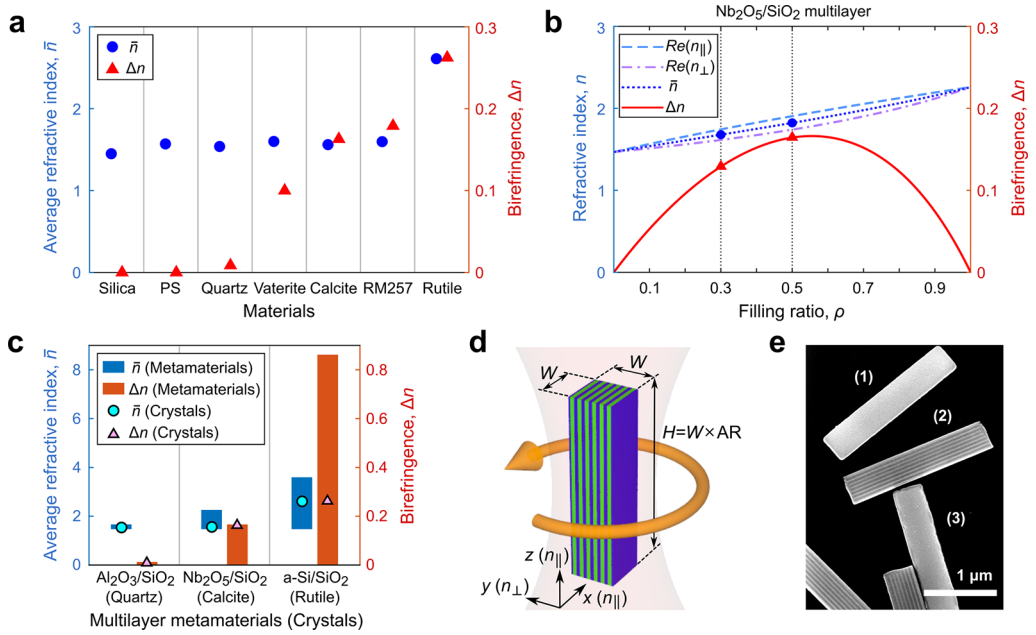

Figure 1. Design principles for MM particles. (a) Optical constants of the most common materials used in optical trapping. For each material, the average refractive index $\bar{n}$ (circle) and optical birefringence Δn (triangle) are shown. (b) EMT-predicted effective indices and birefringence of the Nb_2O_5/SiO_2 multilayer structure as a function of the material filling ratio, ρ. Shown are calculated values for $n_\parallel$ (dashed line) and $n_\perp$ (dash-dotted line), as well as for $\bar{n}$ (= $(n_\parallel + n_\perp)/2$; dotted line) and Δn (= $|n_\parallel - n_\perp|$; solid line). The filling ratios chosen for demonstration and the corresponding optical constants are indicated by the vertical dotted lines and the overlaid symbols (as in panel (a)), respectively. (c) For each MM of different material combination, the EMT-predicted ranges of average refractive index (left-side bar) and birefringence (right-side bar) are shown, together with the optical constants of a natural crystal (overlaid symbols as in legend) that can be emulated by the corresponding MM. (d) Three-dimensional schematic of an MM square-cuboid particle made of Nb_2O_5 (green) and SiO_2 (blue) with its long axis aligned to the propagation direction (z-axis) of the trapping beam (red). Given an input beam linearly polarized along the x-axis, the particle's optic axis ($n_\perp$) aligns with the y-axis, while the axes associated with the higher refractive index ($n_\parallel$) align with the x- and z-axes. The resulting optical birefringence in the x–y plane enables active rotary control around the z-axis (indicated by the curved arrow). The cross section in the x–y plane is a square of width W, and the aspect ratio AR sets the height H along the z-axis. (e) Scanning electron microscopy (SEM) image of MM particles with ρ = 0.3, W = 400 nm, and AR = 5. The three differently oriented particles are marked: bottom (1), side (2), and top (3) (as defined in Figure S10).

degrees of freedom in three dimensions by extra lateral torques.[24,25] However, its very low birefringence (Δn = 0.009)[26] severely limits the maximum torque that can be transferred to it. Although the torque transfer efficiency can be maximized by enlarging the probe, this not only decreases the trapping stability in single-beam optical traps but also reduces the maximum rotational speed and spatiotemporal resolution due to the increased hydrodynamic drag.[23] Although calcite/vaterite $CaCO_3$ crystals have higher birefringence (Δn = 0.1–0.16),[26,27] they are unstable in water and therefore less suited to biological and microfluidic environments. In addition, the possible particle shapes have been limited to irregular fragments for the case of calcite $CaCO_3$[19] and chemically synthesized spheres for vaterite $CaCO_3$.[8,20] Liquid crystal RM257 is stable in aqueous solutions while having similarly high birefringence (Δn = 0.18).[21] However, as in the case of vaterite $CaCO_3$, the possible particle shape of RM257 is limited to spheres.[21]

Meanwhile, another chemically stable material, rutile TiO_2, can be fabricated in top-down fashion into rod-shape particles.[7,22,23] Rutile TiO_2 has the highest birefringence among all the known naturally occurring crystalline materials (Δn = 0.26),[28] and its average refractive index ($\bar{n}$ = 2.6)[28] also exceeds those of other common dielectric probes ($\bar{n}$ = 1.4–1.6).[29,30] As we have demonstrated in ref 23, this combination of high optical index and high birefringence makes it possible, even at only moderate beam powers, to achieve high levels of force and torque transfer efficiencies. Despite its superior properties, rutile TiO_2 does not provide a universal solution for all applications. For example, while the high refractive index of rutile TiO_2 makes it possible to generate high linear stiffness and force, it also results in a large scattering force. To compensate this high scattering force with optical gradient force, a tightly focused trapping beam with a high numerical aperture (NA) objective lens is therefore necessary. Even then, the probe size should be limited to guarantee stable three-dimensional (3D) trapping.[23] These stringent requirements hamper its wide usage, such as in compact and affordable optical trapping systems that often possess low NA optics.[31,32] Furthermore, as the 3D-trapping stability of rutile TiO_2 probes is highly size- and shape-dependent, their use in applications regarding larger sizes or exotic shapes, such as gear-shaped microfluidic rotors,[33,34] would be impractical. Moreover, high trap stiffnesses are not always desirable. Lower trap stiffnesses are intentionally used in certain applications, *e.g.*, photonic force microscopy, where a "soft" probe is beneficial for scanning fragile samples such as cell surfaces.[35]

Therefore, as the optical properties of the currently available birefringent probes do not cover the full application space of optical trapping, there exists a need for a joint force and torque transducer that possesses designed optical constants. Such designed particles could allow one to have any combination of refractive index and birefringence that provides the optimal balance between force and torque transducer properties per

https://dx.doi.org/10.1021/acsnano.0c04233
ACS Nano 2020, 14, 14895–14906

specific application. In addition, they should be chemically stable for demanding applications in aqueous environments. Furthermore, their fabrication should accommodate high uniformity and yield, as well as flexibility in particle geometry. For the previously developed top-down fabrication of quartz SiO_2 and rutile TiO_2 nanoparticles,[14−18,22,23] a crystalline substrate was etched vertically into rod-shaped pillars, which were converted into particles by physically cleaving the base of the pillars. This approach comes with several drawbacks: first, the use of crystalline substrates hampers high volume production, as they are often expensive and only come in small sizes; second, using vertical etching it is challenging to achieve a wide range of aspect ratios for rod-shaped particles;[22] and third, physical cleavage may result in unexpected damage to the particles, degrading their uniformity and reducing yield.

We address all the above-mentioned issues by switching to designed metamaterial particles that can be fabricated in a straightforward manner using robust processes. The choice of metamaterials is motivated firstly by the possibility of tailoring their physical properties beyond the range that exists in naturally occurring materials. For example, metamaterials with artificially defined values of the refractive index[36,37] and birefringence[38] have been demonstrated. Within this context, multilayer metamaterials (MMs) provide a particularly flexible, straightforward means to design and implement desired values of optical constants,[39,40] as the optical properties of MM particles can be customized by pairing materials from the extensive library of diverse amorphous dielectrics and by the layer thickness ratio. As the latter can be tuned in a continuous manner, this allows us to design particles with a nearly arbitrary combination of refractive index and optical birefringence. The choice of metamaterials is motivated secondly by the simplicity of fabrication of MM particles. As we demonstrate below, the fabrication process is robust, compatible with conventional semiconductor fabrication processes, and capable of large-volume production with high uniformity. A multilayer is achieved by sequentially stacking different material layers on a silicon substrate using various thin-film deposition techniques such as sputtering,[41] evaporation,[42] and atomic layer deposition (ALD).[43] Then, the multilayer undergoes lithography and etching to define the dimensions of nanoparticles, which are then harvested in their free-floating form by dissolving the underlying sacrificial layer. Such sacrificial layer-based harvesting is in principle free from undesired deformations in particle geometry,[33,34,44−46] in contrast to the mechanical cleavage-based protocols described above.[14−18,22,23] As the geometry along the long axis of a rod-shaped particle can be lithographically defined and laterally etched, higher aspect ratios can be readily obtained, without the need for thicker or harder etch masks.[22] This also allows for particles with geometries other than rod-shaped, and even includes exotic shapes.[33,34,44] It goes without saying that the use of large-area and cost-effective standard silicon substrates for our MM particles is better suited for mass production compared to natural crystalline substrates.

Using these ingredients, we here demonstrate the realization of birefringent MM particles with tailored optical constants. As a proof of concept, we have designed MMs consisting of niobium pentoxide (Nb_2O_5) and silicon dioxide (SiO_2) that have a large birefringence at only moderate refractive index. The optical constants of the resulting MM particles present all the advantages of calcite/vaterite $CaCO_3$ crystals, while overcoming their known disadvantages such as chemical instability in aqueous environments and the lack of fabrication options for rod-shaped particles. We show using optical trapping experiments that one can achieve highly efficient torque transfer with such 3D-trapped MM particles dispersed in water and compare the experimental performance with theoretical calculations. The utilization of designed MM particles is further facilitated by our robust, sacrificial layer-based top-down fabrication route, which allows high yield, uniformity, and flexibility in particle geometry. Such universal birefringent MM particles, which can be designed either to emulate the properties of existing crystals or to introduce entirely novel ones, would further broaden the applicability of force and torque transducers in optical traps.

RESULTS AND DISCUSSION

Design of Birefringent MM Particles. The design of the artificially birefringent MMs is based on effective medium theory (EMT).[47] EMT predicts that a multilayer of alternating isotropic dielectric materials exhibits an effective birefringence. When the thickness of each layer is much smaller than the wavelength of the incident electromagnetic wave, the effective optical permittivity of the structure can be approximated by a tensor:

$$\underline{\epsilon} = \begin{bmatrix} \epsilon_{\parallel} & 0 & 0 \\ 0 & \epsilon_{\parallel} & 0 \\ 0 & 0 & \epsilon_{\perp} \end{bmatrix} \tag{1}$$

where $\epsilon_{\parallel}$ and $\epsilon_{\perp}$ are the permittivity components parallel and perpendicular to the interfacial surfaces of the multilayer stack, respectively. Their values are given by

$$\epsilon_{\parallel} = \rho\epsilon_1 + (1-\rho)\epsilon_2 \tag{2}$$

$$\epsilon_{\perp} = 1/(\rho\epsilon_1^{-1} + (1-\rho)\epsilon_2^{-1}) \tag{3}$$

where ϵ_1 and ϵ_2 are the permittivity values of the higher- and lower-index materials, respectively, and the material filling ratio $\rho = d_1/(d_1 + d_2)$ is defined as the thickness ratio of the higher-index material layer (d_1) and the unit layer-pair ($d_1 + d_2$).

As a primary method to validate the accuracy of the EMT approximation for the optical properties of MM, we compare the Fresnel coefficients calculated from the approximated homogeneous single-layered structure, whose effective optical constants are calculated using EMT (eqs 1−3), with those from the actual multilayered structure[48] (Figure S1). We find that the Fresnel coefficients calculated from the effective single-layer geometry approximate those of the multilayer geometry for both p- and s-polarizations of the incident beam (Figure S1) provided that the number of layer-pairs exceeds 2, confirming that EMT is sufficiently precise to describe our MMs. We additionally validated the EMT prediction by calculating the optical trapping forces and torques using finite element methods (FEM) (Figure S2; Methods).

For the constituent materials of MMs, we focus on dielectric materials that are commonly used in thin-film deposition techniques (*e.g.*, evaporation, sputtering, and ALD) and able to form stable multilayer compositions. For most of such dielectric materials, there are well-developed surface functionalization protocols[49−51] that could facilitate the use of MMs in diverse areas including biological applications. As a proof of concept, we searched for promising combinations of high- and low-index material pairs for MMs, with the goal of obtaining an

https://dx.doi.org/10.1021/acsnano.0c04233
ACS Nano 2020, 14, 14895−14906

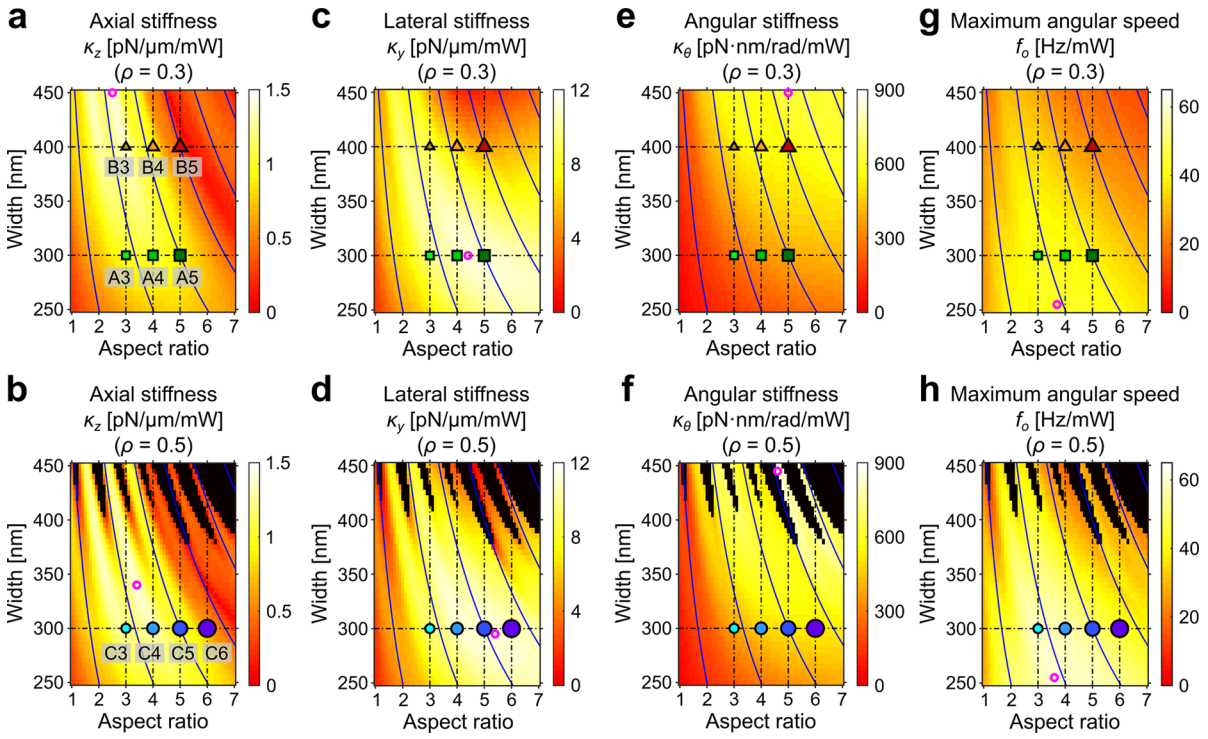

Figure 2. Calculated maps of the trapping stiffnesses and maximum angular speeds for MM nanocuboids. FEM-calculated maps for (a, b) the axial stiffness κ_z, (c, d) the lateral stiffness κ_y, (e, f) the angular stiffness κ_θ, and (g, h) the maximum angular speed f_o are shown as a function of aspect ratio AR and width W of the Nb_2O_5/SiO_2 MM nanocuboids with filling ratios of ρ = 0.3 (panels (a, c, e, g)) and ρ = 0.5 (panels (b, d, f, h)). The directions of linear (panels (a−d)) and angular (panels (e−h)) trapping are indicated by the coordinate system and the curved arrow, respectively, as shown in Figure 1d. All trapping parameters presented are calculated for the case of an input beam that is linearly polarized along the x-axis and the specific configuration of the employed OTW setup (Methods) and then normalized by the theoretically calculated input laser beam power (Methods). In all maps, the solid blue lines represent contour lines for nanocuboids of constant height that range from 500 nm (leftmost) to 3000 nm (rightmost) at intervals of 500 nm, and the pixel size is ΔAR = 0.1, ΔW = 5 nm. The particle dimensions that correspond to the maximum for each map are indicated by the empty magenta circles. The black pixels in the maps of ρ = 0.5 (panels (b, d, f, h)) indicate the particle dimensions that cannot be trapped in 3D due to excessive scattering forces. The 10 different particle dimensions (A3−5, B3−5, and C3−6) chosen for demonstration are indicated by the crossing-points of the black dash-dotted lines, overlaid with corresponding symbols in each map, and their labels are displayed in panels (a) and (b).

MM with a large birefringence at only moderate refractive index, a combination of optical properties also found in $CaCO_3$ crystals (Figure S3). We examined several high-index materials as potential partners for the low-index material SiO_2 and ultimately chose Nb_2O_5. The resulting Nb_2O_5/SiO_2 multilayer emulates the optical constants of both calcite and vaterite $CaCO_3$ crystals (Figure S3) and comes with reliable fabrication (as demonstrated in other optical applications[52]). Using plasma-assisted reactive magnetron sputtering, we are able to deposit Nb_2O_5/SiO_2 multilayers with precisely controlled thickness and refractive indices (n = 1.47 for SiO_2 and n = 2.26 for Nb_2O_5 at 1064 nm) (Methods).

Using EMT, the optical properties of this multilayer combination can be predicted as a function of material filling ratio ρ (eqs 1−3). One can observe in Figure 1b that the refractive index along the ordinary axes ($n_o = n_{\parallel} = \sqrt{\epsilon_{\parallel}}$) exceeds that along the extraordinary axis ($n_e = n_{\perp} = \sqrt{\epsilon_{\perp}}$), indicating that the Nb_2O_5/SiO_2 multilayer emulates a negative uniaxial birefringence ($n_e < n_o$). From these indices, the multilayer's full tunable range for the magnitude of the effective birefringence ($\Delta n = |n_e - n_o|$) and the corresponding average refractive index ($\overline{n} = (n_e + n_o)/2$) can be obtained. The value of the birefringence (Δn) can be fixed anywhere between zero and its maximum value (Δn = 0.17 when ρ = 0.55), while the value of index ($\overline{n}$) varies between 1.47 (that of SiO_2) and 2.26 (that of Nb_2O_5). Except at the maximum birefringence, there are two distinct filling ratios (and hence two different average indices) that achieve the same degree of birefringence (Figure 1b). This allows for a trade-off between 3D-trapping stability and maximum achievable force: a smaller index renders the MM particle more easily trapped in 3D due to the reduced scattering force, while a larger index enhances the gradient force due to the increased index contrast with the surrounding medium (*i.e.*, water, in our experiments). Depending on the target application or experimental situation, one can determine the suitable filling ratio to obtain a desired combination of refractive index and birefringence for MM particles.

We have selected two different filling ratios for Nb_2O_5/SiO_2 multilayers (Figure 1b) to demonstrate the tunability of the optical constants in our MMs and thus the ability to emulate diverse birefringent crystals. We first select ρ = 0.5 (close to the value of ρ = 0.55 that maximizes birefringence) to demonstrate a birefringence (Δn = 0.16) as large as that of calcite $CaCO_3$. We also select ρ = 0.3 with the goal of achieving a lower refractive index ($\overline{n}$ = 1.68, compared to $\overline{n}$ = 1.82 at ρ = 0.5) while maintaining a high level of birefringence (Δn = 0.13). Further decrease of the material filling ratio to ρ = 0.2 should result in lower values for the index ($\overline{n}$ = 1.61) and birefringence (Δn = 0.10) that are comparable to those of

https://dx.doi.org/10.1021/acsnano.0c04233
ACS Nano 2020, 14, 14895−14906

vaterite $CaCO_3$. We note that for Nb_2O_5/SiO_2 MMs, values of $\rho < 0.55$ realize the combination of moderate index and high birefringence, similar to calcite/vaterite $CaCO_3$ crystals ($\bar{n} \approx 1.6$; $\Delta n = 0.1-0.16$);[26,27] if higher values of the linear trapping stiffness are desired for the same degree of birefringence, then a higher filling ratio ($\rho > 0.55$) should be employed (Figure 1b). As can be seen in Figure 1c, numerous other material combinations can also be employed to fabricate MMs with properties either similar to those of existing crystals or going beyond them. For example, the predicted optical constants of MMs composed of aluminum oxide (Al_2O_3) and SiO_2 multilayer pairs can mimic those of quartz SiO_2. Meanwhile, MMs composed of amorphous silicon (a-Si) and SiO_2 multilayer pairs could either emulate the optical properties of rutile TiO_2 (the most birefringent crystal found in nature, with $\Delta n = 0.26$) or access even 3-fold higher values of the birefringence ($\Delta n = 0.86$).

Based on this multilayer structure, the MM particle geometry was designed. To ensure full three-dimensional rotational confinement of each MM particle, the particle is rod-shaped with a high aspect ratio (AR). The high AR generates sufficiently large lateral torques to maintain the particle's orientation with its long axis aligned to the direction of laser beam propagation (z-axis) in an optical trap as shown in Figure 1d, unless their sizes are much smaller than the waist of the focused beam.[24,25] As the particle's optic axis ($n_\perp$) is perpendicular to its longer side (Figure 1d), active rotary control of the particle around the z-axis can then be achieved by exploiting its optical birefringence in the $x-y$ plane and rotating the linear polarization of the trapping beam.[6] In our top-down fabrication (Figure 1e, Methods), we have confined our particle shape to be square-cuboid to assess only the torque induced by optical birefringence. While the cross section of a square-cuboid in the $x-y$ plane is not fully rotationally symmetric (unlike that of a cylinder[16,22]), compared to a rectangular-cuboid or other possible geometries it is relatively free of unwanted geometrical torques that would affect rotation about the z-axis and hinder precise angular control and detection.

Numerically Calculated Trapping Performance of MM Particles. We have performed FEM calculations of the linear and angular optical trapping landscapes (Methods) to underpin our design of MM particles. Here, we demonstrate the results for the case of Nb_2O_5/SiO_2 MM particles, with two chosen material filling ratios ($\rho = 0.3$ and $\rho = 0.5$; Figure 1b). We vary the width W of nanocuboids over a range of 250–450 nm, while we examine AR ranging from 1 (cubes) to 7 (square cuboids with increasing heights).

To predict the 3D-trapping stability for MM nanocuboid particles, we have calculated the axial stiffness κ_z for $\rho = 0.3$ and $\rho = 0.5$ and plotted this in a heat map (Figure 2a,b). For each particle dimension, κ_z is defined as the slope of the axial force curve (Figure S2) at the equilibrium trapping position z_{eq} (Figure S4). The nanocuboids with $\rho = 0.3$ are trappable over the entire range of widths and aspect ratios in the map. In contrast, the nanocuboids with $\rho = 0.5$ include nontrappable dimensions which appear at $W \gtrsim 375$ nm and are displayed as black pixels in Figure 2b; in such cases, the axial stiffnesses cannot be defined, as the dominant scattering forces result in an absence of z_{eq}. Calculations at the corresponding dimensions were not carried through and are thus also displayed as black pixels in Figure 2d,f,h. Additional calculations in which W is extended up to 550 nm (Figure S5) show that the nanocuboids with $\rho = 0.3$ become nontrappable at $W \gtrsim 525$ nm. The much narrower range of 3D-trappable dimensions for MM particles with $\rho = 0.5$ (also reflected by the occurrence of maximal stiffness values at far smaller widths; compare the positions of the magenta circles in Figure 2a,b) results from the larger scattering forces that derive from their higher average refractive index ($\bar{n} = 1.82$, compared to $\bar{n} = 1.68$ for $\rho = 0.3$).

We also calculated the lateral stiffness κ_y (Figure 2c,d) at z_{eq}, which generally exhibits larger values than κ_x when the input beam is linearly polarized along the x-axis and a subwavelength-sized particle is trapped.[53] Overall, the lateral stiffness κ_y is almost an order of magnitude larger than the axial stiffness κ_z and maximized around $W \approx 300$ nm (magenta circles in Figure 2c,d), regardless of the filling ratio. We attribute such a common optimal particle width (~300 nm) for the maximal lateral forces to an ideal degree of overlap between particle and field gradient profile of the focused beam in the lateral direction.

The calculated maps of angular stiffness κ_θ (Figure 2e,f) at z_{eq} represent the maximum torque ($\tau_o = \kappa_\theta/2$) experienced by each particle rotated 45° with respect to the direction of the input beam linear polarization.[54] Overall, within the range of dimensions shown in the maps, a larger angular stiffness can be achieved with particles with higher aspect ratios for a given width, which can be explained by the dependence of torque transfer efficiency on particle height.[23] When we compare the values of the angular stiffness for particles with $\rho = 0.5$ *versus* $\rho = 0.3$ (with otherwise identical dimensions), we find that the maximum angular stiffness in each map (magenta circles in Figure 2e,f) is larger for particles with $\rho = 0.5$ (877 pN·nm/rad/mW) *versus* $\rho = 0.3$ (653 pN·nm/rad/mW). This difference results from their higher birefringence (by 27%) and ensures a higher torque transfer efficiency for these particles.

Although the angular stiffness of the $\rho = 0.5$ nanocuboids can be maximized by selecting particle dimensions in the finger-shaped regions[55] at the top of the map (*e.g.*, magenta circle in Figure 2f), in practice their utilization in 3D trapping is difficult. Due to variation in particle dimensions within a batch, some fraction of particles will lie outside of the finger-shaped region, adopting dimensions that do not support 3D trapping. Also, the nonidealities of the actual trapping system (*e.g.*, aberrations of the trapping beam) will modify the trapping landscape (*e.g.*, shift the finger-shaped regions or threshold width for 3D trapping);[23] hence, even particles fabricated to high uniformity might have reduced stiffness or become nontrappable. In contrast, due to their lower refractive index, nanocuboids with $\rho = 0.3$ are predicted to be trappable for all dimensions shown in the map, including those with the dimensions that maximize angular stiffness (*e.g.*, magenta circle in Figure 2e).

Using these FEM-calculated maps of angular stiffness κ_θ (Figure 2e,f), together with the map for the rotational drag coefficient γ_θ (Figure S6), we generate maps for the predicted maximum angular speed f_o ($= (\kappa_\theta/2)/(2\pi\gamma_\theta)$) of the nanocuboids (Figure 2g,h). Overall, higher angular speeds are achieved for particles with smaller widths at fixed heights (and thus similar torque transfer efficiencies), which makes sense as the rotation of larger particles is hindered by increased rotational drag in the surrounding medium (water). The angular speeds of nanocuboids with $\rho = 0.5$ are higher compared to similarly sized nanocuboids with $\rho = 0.3$

https://dx.doi.org/10.1021/acsnano.0c04233
ACS Nano 2020, 14, 14895–14906

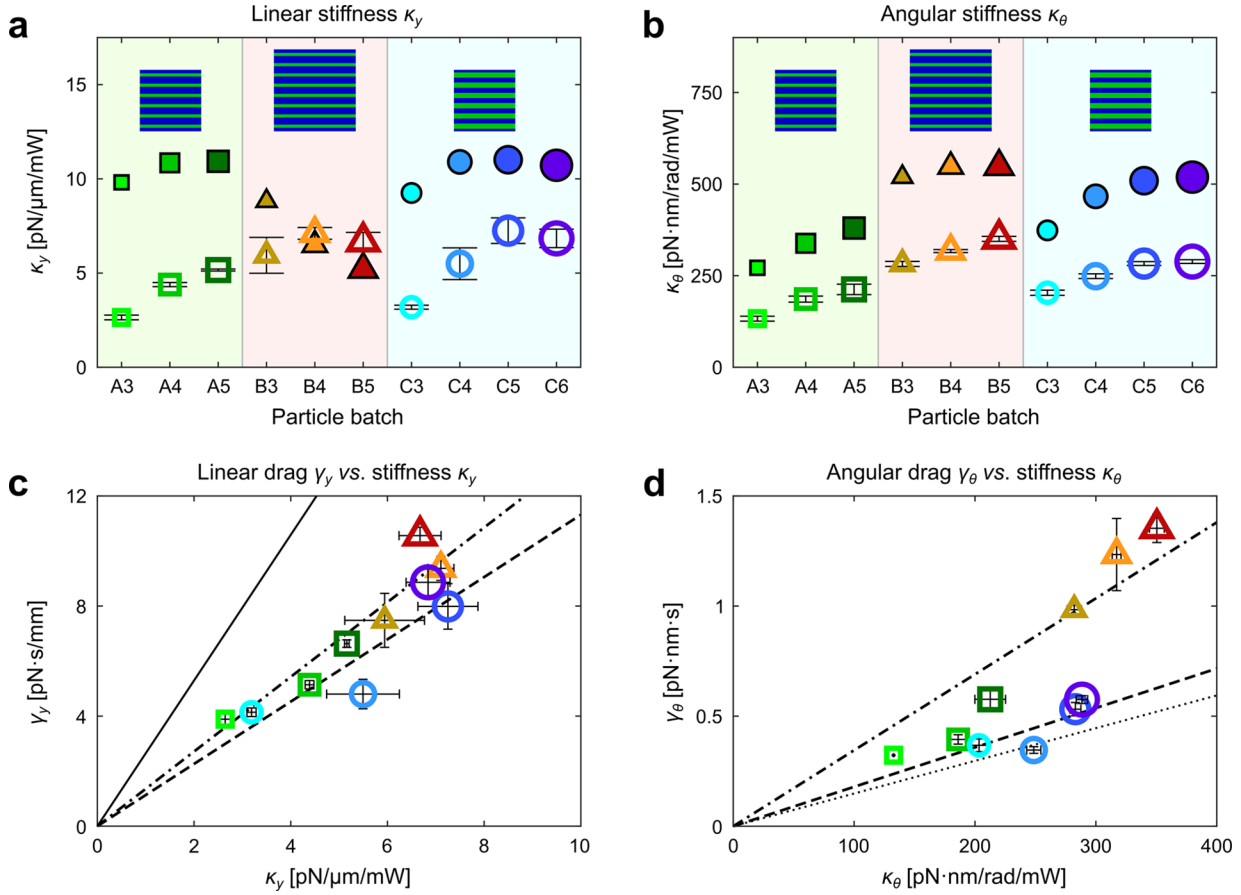

Figure 3. Measured linear and angular trapping stiffnesses and drag coefficients for MM nanocuboids in an OTW. The OTW-measured (a) linear stiffness κ_y and (b) angular stiffness κ_θ are shown for all 10 batches of MM nanocuboids (A3 to C6). The measured stiffness values are normalized by the precisely calibrated actual input laser beam power (Methods). The empty symbols and the error bars denote the mean and the standard deviation for each batch, while the corresponding FEM-predicted values (taken from the maps of Figure 2c,d,e,f) are shown as filled symbols. The three different groups of MM nanocuboid batches (A, B, and C) are indicated by the color shading and the schematics of particle cross section along the $x-y$ plane (defined as in Figure 1d) that illustrate different film thicknesses and material filling ratios (color-coded as in Figure 1d and structured as in Table S1). (c, d) The OTW-measured stiffnesses (κ) shown in panels (a) and (b) are plotted against the corresponding OTW-measured drag coefficients (γ) (empty symbols and error bars, the same color coding as in panels (a) and (b)). The characteristic response time ($t_c = \gamma/\kappa$) for each filling ratio ρ is deduced from the slope of the linear fit to the corresponding data points (forced through the origin; dash-dotted lines for $\rho = 0.3$; dashed lines for $\rho = 0.5$). For comparison, the fit to the linear stiffness *versus* drag data for PS beads is shown as a solid line in panel (c), and the fit for angular data of rutile TiO_2 cylinders is shown as a dotted line in panel (d) (measured in ref 23 under identical conditions). The data in panels (a)−(d) are summarized in Table S2.

(compare the magenta circles at 61 Hz/mW and 45 Hz/mW in Figure 2h,g, respectively), reflecting the enhanced angular stiffnesses of particles with $\rho = 0.5$.

On the basis of these results, we selected our MM particle dimensions for each filling ratio and designed three different multilayer wafers for their fabrication. We deposited two multilayers with $\rho = 0.3$, with widths W of 300 nm (wafer A) and 400 nm (wafer B), respectively, and one multilayer with $\rho = 0.5$, with a width W of 300 nm (wafer C) (Table S1). The smaller width $W = 300$ nm is selected because for both filling ratios it combines stable axial trapping (Figure 2a,b) with maximal lateral trapping (Figure 2c,d). It thus allows for an examination of trapping behavior as a function of filling ratio for identically sized, 3D-trapped particles. For example, $\rho = 0.5$ particles, having higher birefringence than $\rho = 0.3$ particles, are expected to achieve both higher torques and angular speeds at $W = 300$ nm (Figure 2e,f,g,h). To explore the trapping behavior of particles with much larger volumes, we also selected the larger width $W = 400$ nm for $\rho = 0.3$ (Figure 2a) (particles of this width not being stably 3D-trappable for $\rho = 0.5$; Figure 2b). Particles with this width are predicted to exhibit larger torques but slower angular speeds than particles with $W = 300$ nm (Figure 2e,f,g,h). For all three wafers, we fixed the thickness of the unit layer-pair to 50 nm to enable the use of EMT in predicting the effective optical constants for the designed multilayer particle widths by allowing a sufficiently large number of layer-pairs (6 or 8, Figure S1) and to provide reliable control of the selected filling ratios by defining the thinnest layer to exceed ~10 nm (Table S1), large compared to the nanometer-scale precision of our multilayer deposition (Methods). Regarding the particle height, we fabricated particles with AR of 3, 4, and 5 for all three wafers, where the range is selected to probe the height-dependence of the torque transfer efficiency while ensuring full three-dimensional rotational confinement. The resulting particle heights span the range of $H \approx 1-2$ μm and thus include heights predicted to achieve torque transfer efficiencies close to 100%, *i.e.*, $H = 2.0$ μm for $\rho = 0.3$ ($W = 400$ nm, AR = 5) and $H = 1.5$ μm for $\rho = 0.5$ ($W = 300$ nm, AR = 5) (Figure S7). Lastly, to explore the torsional behavior of particles with heights exceeding those

https://dx.doi.org/10.1021/acsnano.0c04233
ACS Nano 2020, 14, 14895−14906

predicted to optimize torque transfer efficiency, we also fabricated a particle batch with H = 1.8 μm for ρ = 0.5 (W = 300 nm, AR = 6). The dimensions for 10 designed particle batches (A3−5, B3−5, and C3−6, where the letter and number represent the wafer and the aspect ratio, respectively) are indicated on the maps in Figure 2a,b.

The MM nanocuboid dimensions are not limited to the above-mentioned size ranges and can be enlarged or reduced as necessary. The upper boundary of particle dimensions, of interest in, for example, diverse microfluidic components,[33,34] is set by the 3D-trappable regime for each chosen filling ratio. The lower boundary, which can be beneficial to achieving improved precision in single-biomolecule measurements,[7] is determined by the specific design constraints for MM particles, namely, (i) the thinnest layer of a multilayer stack should be sufficiently thick to ensure reliable and reproducible multilayer deposition (Methods, Table S1); (ii) the number of layer-pairs should exceed 2 to permit usage of the EMT approximation in particle design (Figure S1); and (iii) the particle length should not be substantially smaller than the waist of the focused beam and should exceed the particle width (*i.e.*, maintain a high aspect ratio) to achieve the proper trapping orientation (Figure 1d). Conforming to these criteria, the precision of multilayer deposition (∼1 nm) and the resolution of patterning (∼10 nm) in our fabrication environment (Methods) are sufficient to achieve even sub-100 nm particle width while a sufficiently long particle height is readily defined by lithography.

Linear and Angular Trapping Behavior of MM Particles. We have fabricated and characterized 10 batches of Nb_2O_5/SiO_2 MM particles. The fabrication process (Methods; Figures S8−S10, Table S1) was tuned to produce particles with actual dimensions as close as possible to the design parameters with high uniformity, resulting in <3% relative standard deviations (RSD = SD/mean × 100) in each dimension (Figure S10). To measure the linear and angular trapping properties of these different particles, we then introduce them into an optical torque wrench (OTW) setup[23] (Methods; Figures S11, S12, Table S2).

We first confirmed the tight 3D-trapping of the MM nanocuboids by measuring linear trapping properties along all principal axes (x, y, and z) (Figure S12). Overall, the nanocuboids show the highest stiffness along the y-axis (κ_y), and we use this parameter for further analysis and comparison (Figure 3a). We next characterized the angular operation of each 3D-trapped nanocuboid about the z-axis, which is controlled by the linear polarization direction of the input beam, and computed the resulting values of the angular stiffness (Figure 3b). Within each batch, the particles behave similarly, with average RSD values of ∼6% in the measured linear and angular parameters (RSD ≈ 1−14% for stiffness and RSD ≈ 2−13% for drag). These RSD values are as low as those obtained for highly uniform commercially available PS beads in the same setup (RSD ≈ 7−11% for stiffness and RSD ≈ 7−9% for drag),[23] which confirms that the fabricated nanocuboids are highly uniform in both optical properties and geometry.

We then compared the OTW-measured linear and angular trapping properties of the MM nanocuboids with our FEM calculations. The measured linear and angular stiffnesses show quantitative agreement with the corresponding values calculated using FEM, provided that the latter are scaled by 0.63 ± 0.31 for κ_y (Figure 3a) and 0.55 ± 0.04 for κ_θ (Figure 3b) (mean ± SD; for the measured particles in all batches). Such scaling factors are expected, as similar factors have been observed for other types of particles probed in the same setup (∼0.58 for PS beads and ∼0.42 for rutile TiO_2 cylinders).[23] We attribute the necessity for scaling to the fact that the FEM calculations do not take into account optical aberrations, which can substantially distort the field gradient of the tightly focused trapping beam.[56] Furthermore, for the particle batches from wafer B, the increased sensitivity to optical aberrations of linear trapping over angular trapping accounts for the increased variability in the scaling factor for lateral stiffness (Figure 3a) over angular stiffness (Figure 3b). This can be attributed to (i) their larger diameters (400 nm), which make it likely that the particle−medium interface lies at the boundary of the focused beam where the field gradient is more susceptible to optical aberrations and (ii) their likely more negative values for equilibrium trapping positions z_{eq} (Figure S4), which leads them to experience a larger field gradient than those trapped at positive z_{eq} values if optical aberrations render the shape of the focused beam axially asymmetric.[57]

Scaling factors are also required to achieve quantitative agreement between experimentally measured linear and angular drag coefficients and the predictions made by FEM: the calculated drag coefficients are scaled by 0.84 ± 0.14 for γ_y and 0.70 ± 0.08 for γ_θ (Figure S12). Here, the requirement for scaling likely results from differences between the actual geometries of nanocuboids (which have rounded edges when fabricated; Figure S8) compared to the idealized geometries with sharp edges in our FEM modeling (Methods). Indeed, rotationally symmetric particle geometries measured in the same setup[23] exhibit near-unity scaling factors for the drag coefficients (*e.g.*, spherical beads, scaling factor ∼1.02; cylindrical rods, scaling factor ∼1.04).

The highly consistent agreement between our experiments and calculations for the linear/angular drag coefficients and angular trapping stiffness in all particle batches (Figure S12) proves that the particle geometries and optical properties conform to design, reinforcing the notion that mismatches found in the experimental measurements of linear trapping stiffnesses for several particle batches result from optical aberrations. This also proves that all of the tested nanocuboids are actually trapped in an optical trap with the orientation as shown in Figure 1d,[24,25] as otherwise the experimental results would have been inconsistent with the calculations that assume the idealized situation depicted there.

By examining our experimental results for MM particles with different material filling ratios, we could clearly demonstrate the ability to tune their optical constants. The particles in batches A3−5 and C3−5 have the same geometry (W = 300 nm, AR = 3−5) and hence in principle the same drag coefficients; indeed, the ratio of their measured drag coefficients is 1.00 ± 0.13 ((batches C3−5)/(batches A3−5); Figure S12). However, the particles in batches C3−5 (ρ = 0.5) exhibit measured linear and angular stiffnesses that are ∼29% and ∼40% higher than particles in batches A3−5 (ρ = 0.3), respectively (Figure 3a,b). As these results are in accordance with the predictions for the optical constants from EMT (Figure 1b), we attribute these differences to their different material filling ratios.

We illustrate how the ability to tune optical constants of MM particles can be beneficial by showing how it can be used to maximize achievable torques. For example, increasing values of the AR results in higher torques for particles with ρ = 0.5 (batches C3−5 in Figure 3b); however, the efficiency of torque transfer subsequently saturates, as shown by the modest

https://dx.doi.org/10.1021/acsnano.0c04233
ACS Nano 2020, 14, 14895−14906

increase in angular stiffness upon further increase of the AR (compare batches C5 and C6 in Figure 3b). If higher torques are desired, then increasing the particle width W can be considered. This approach is limited for particles with $\rho = 0.5$, as only a narrow range of widths is compatible with stable 3D-trapping (Figure 2b). Tuning the optical constants provides an alternative: the lower index of multilayers with $\rho = 0.3$ expands the range of 3D-trappable particle dimensions while retaining high birefringence, allowing the stable trapping of larger particles and hence the generation of larger torques. Thus, particles with $\rho = 0.3$, the larger width $W = 400$ nm, and a height close to the theoretical optimum for 100% torque transfer efficiency (batch B5) allow for a ~23% larger measured torque compared to similarly optimized particles with $\rho = 0.5$ and smaller width $W = 300$ nm (batches C5−6), as shown in Figure 3b.

A further parameter with which we can compare the trapping performance of MM particles is the response time t_c, which is defined as the ratio of the measured drag and stiffness (*i.e.*, the slope of the fitted lines in Figure 3c,d). We fit the data sets for MM particles of different material filling ratios and benchmark their response times against those of PS beads and rutile TiO_2 cylinders measured in the same setup.[23] For facile comparison, each response time is shown for a reference value of 100 mW beam power in the optical trap, scaled from the measured values obtained at 92 mW. By comparing the linear response times for MM particles with $\rho = 0.5$ ($t_{c,y} \approx 11$ μs) and $\rho = 0.3$ ($t_{c,y} \approx 14$ μs), we confirm that these reflect the differences in their refractive indices ($\bar{n} = 1.82$ and 1.68, respectively). As expected, both linear response times are shorter than that of PS beads with a lower refractive index ($t_{c,y} \approx 26$ μs for $n = 1.45$). Meanwhile, differences in the angular response times of MM particles reflect differences in their birefringence, as shown by the 2-fold faster response of MM particles with $\rho = 0.5$ ($t_{c,\theta} \approx 18$ μs; $\Delta n = 0.16$) compared to those with $\rho = 0.3$ ($t_{c,\theta} \approx 35$ μs; $\Delta n = 0.13$). Both angular response times are longer than that of rutile TiO_2 cylinders with a higher birefringence ($t_{c,\theta} \approx 15$ μs; $\Delta n = 0.26$). Importantly, the distinguishable linear and angular response times of the MM particles with $\rho = 0.3$ and $\rho = 0.5$ again confirm that the index and the birefringence of multilayer structures can both be tuned by choosing different material filling ratios.

We complete our investigation of the angular trapping behaviors of Nb_2O_5/SiO_2 MM particles by plotting their full torque−speed curves (Figure 4; measured at 92 mW beam power in water) and benchmarking their torque−speed performance relative to single-crystal rutile TiO_2 cylinders (magenta stars in Figure 4; data from ref 23). Here, the optical torque is plotted as a function of the linear polarization rotation frequency (PRF) of the input beam. One initially observes a linear regime in which torque rises as PRF is increased (and the particle rotates more rapidly), followed by a nonlinear regime in which the average torque decreases as PRF is increased (and the particle rotation becomes more asynchronous with PRF).[54] The measured optical torques excellently fit to the analytical equations in both the linear and nonlinear regimes[54] (overlaid black lines in Figure 4). The slope of the linear part of each curve represents the particle's angular drag coefficient ($\gamma_\theta = \tau_o/(2\pi f_o)$). As evidenced by their nearly identical slopes, particles in batches A3−5 (green squares) and C3−5 (cyan to violet circles) have similar angular drag coefficients, as expected from their identical design

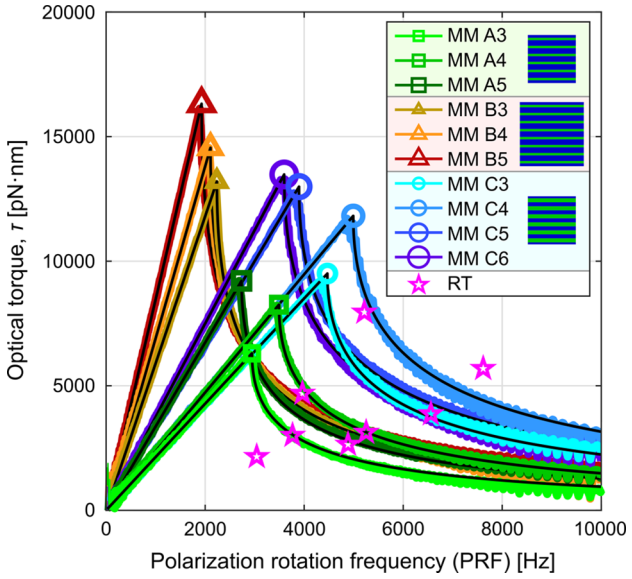

Figure 4. Measured optical torque transduced by MM nanocuboids in an OTW. The optical torques transduced by single optically trapped MM nanocuboids in water (one particle per batch) *versus* input beam polarization rotation frequency (PRF) as measured in an OTW. The laser power at the optical trap is ~92 mW. The moving-average torque signals are displayed as colored solid lines, and the corresponding fits to the theoretically predicted response[54] are overlaid as black solid lines. The maximum torque−speed data points are marked by the corresponding symbols (see legend; color coding of symbols, color shading, and MM nanocuboid cross sections are the same as in Figure 3a,b). Until the maximum torque is reached, the angular speed (f) of the trapped particle is identical to the PRF of the laser beam, and it is proportional to the optical torque (τ), with the angular drag (γ_θ) as the proportionality constant ($\tau = 2\pi\gamma_\theta f$). When the PRF exceeds the maximum angular speed of a particle, the particle rotation becomes more asynchronous to the PRF, resulting in a lower average torque.[54] For comparison, the maximum torque−speed values of eight differently sized single rutile TiO_2 (RT) nanocylinders are overlaid (magenta stars; measured in ref 23 under identical conditions). The small spikes near zero PRF and the ripples at high PRF are attributed to artifacts of the measurement method.[23]

geometries. The higher birefringence of wafer C than wafer A ($\rho = 0.5$ *versus* $\rho = 0.3$, respectively), however, allows one to access higher maximal torques and angular speeds for particles from batches C3−5. Meanwhile, as can be deduced by their discernibly steeper slopes, particles from batches B3−5 (yellow to red triangles) have increased angular drag coefficients compared to particles from batches A3−5 and C3−6, as expected from their larger volumes. The highest torques were achieved with particles from wafer B ($\rho = 0.3$), facilitated by the larger particle sizes compatible with stable 3D-trapping at this filling ratio (but resulting in their concomitantly lower values for the maximal rotation speeds). Thus, we observe that the generation of high torques is facilitated by either high birefringence or large (trappable) particle size, but in the latter case comes at the expense of a reduced temporal response.

When compared to single-crystal rutile TiO_2 cylinders measured under the same conditions, we observe that our Nb_2O_5/SiO_2 MM particles can achieve up to ~2 times higher maximum torque (compare 16.3 nN·nm for MM particles with $\rho = 0.3$ and 13.5 nN·nm for MM particles with $\rho = 0.5$, to 8.0 nN·nm for rutile TiO_2). While the MM particles have a

https://dx.doi.org/10.1021/acsnano.0c04233
ACS Nano 2020, 14, 14895−14906

lower value of the birefringence (Δn = 0.13−0.16 *versus* Δn = 0.26 for rutile), this can be compensated through the use of larger volumes. Such larger volumes, which result in a lower maximum angular speed for Nb_2O_5/SiO_2 MM particles (3.5 kHz for ρ = 0.3; 5.0 kHz for ρ = 0.5) compared to rutile TiO_2 cylinders (7.6 kHz), are permitted since the threshold width for stable 3D trapping of our Nb_2O_5/SiO_2 MM particles (~525 nm for ρ = 0.3, Figure S5; ~375 nm for ρ = 0.5, Figure 2b) exceeds the threshold diameter of ~255 nm for rutile TiO_2 cylindrical particles.[23]

CONCLUSIONS

In this work, we have demonstrated a robust approach to the design and fabrication of multilayer metamaterial nanoparticles for force and torque transduction in optical trapping applications. We have validated the accuracy of the EMT approximation for predicting the optical constants of multilayer structures using analytical and numerical calculations. From among the many potential materials, we selected Nb_2O_5 and SiO_2 as the multilayer material pair for experimental demonstration of our approach. We modeled the linear and angular trapping properties of square-cuboid MM nanoparticles as a function of particle dimension and material filling ratio using FEM calculations and fabricated selected nanocuboid designs by etching into a multilayer stack composed of alternating Nb_2O_5 and SiO_2 layers. The nanocuboids are released from their substrate by dissolution of an underlying sacrificial layer to produce freely floating particles that remain stable in aqueous environments. By capturing such particles in an optical torque wrench and measuring their linear and angular trapping properties, we could experimentally deduce their high uniformity in size and composition from the low variability in their trapping properties. Importantly, we could demonstrate the tunability of optical constants. As such, we could realize MM nanoparticles that emulate the optical properties of calcite/vaterite $CaCO_3$ crystals, while avoiding the physicochemical limitations of these crystals that have prevented them for achieving their full potential. We could also show that the trapping properties of differently designed MM particles could be tuned and understood: MM particles with higher material filling ratios exhibited higher linear and angular stiffnesses, and shorter response times, compared to particles of identical dimensions but lower material filling ratios; similarly, such particles could be rotated fastest, at speeds up to ~5 kHz in water. The highest torques (~16 nN·nm) were obtained for particles with lower material filling ratios, as their lower index enables stable 3D-trapping of larger dimensions. These maximal torques are 2-fold larger compared to that achieved with rutile TiO_2 nanocylinders, which have higher birefringence but require smaller dimensions to remain trappable in 3D, and moreover are more challenging to fabricate.

Our MM particles have many advantages over existing materials for optical trapping applications. First, the above-mentioned tunability allows one to circumvent the limited set of optical constants accessible with naturally occurring materials and design new types of nanoparticles to, for example, access broader regimes of force and/or torque transduction. For example, large, highly birefringent, yet 3D-trappable MM particles, such as those derived from our Nb_2O_5/SiO_2 multilayer with ρ = 0.3, are promising as powerful rotating microfluidic components.[34] Moreover, there exist specific material combinations beyond the Nb_2O_5/SiO_2 pair presented here to further expand the accessible range of optical constants: the a-Si/SiO_2 pair, for example, is expected to achieve exceptionally high birefringence. Second, our MMs allow for chemical stability (by pairing materials stable in aqueous environments), particle harvesting in water, and various options for surface functionalization,[45,49−51] properties that are beneficial for microfluidics and biological applications such as studies of rotary motors[58] and torque−response of biomolecules.[5−7] Third, due to the orientation of the optic axis normal to the multilayer substrate surface, the particle geometry along the long axis is lithographically defined, presenting no practical limitation on particle height or shape.[44] In contrast, the fabrication of particles from birefringent substrates with an in-plane optic axis requires vertical etching, making it a challenge to realize particles with heights exceeding 1−2 μm or with unconventional sidewall shapes, particularly for hard-to-etch crystals.[22] The ease of realizing a longer particle is a notable advantage for torque transducers, as the optical torque transfer efficiency is largely dependent on particle height. For example, the maximal achievable torque and rotation frequency are 2-fold larger for a circularly polarized rather than a linearly polarized input beam, provided that the particle height can be made 2-fold longer than the optimal height for a linearly polarized input beam.[6] Fourth, unlike single-crystal substrate-based fabrication (*e.g.*, quartz SiO_2 or rutile TiO_2),[16,22] our sacrificial layer-based fabrication utilizes standard silicon substrates and does not require mechanical cleavage of particles. As such, it guarantees uniform particle geometry and can be extended to mass production. This high yield and uniformity are beneficial for many torque-related biological[7] and physical[8] experiments, in which a large number of identical particles is desired to obtain statistically sound and reproducible results. Together, the designable optical properties and versatile fabrication of universal birefringent MM particles target them as highly promising candidates for future development of optimized, high-performance optomechanical transducers for use in science and engineering.

METHODS

Finite Element Method Modeling of Optical Trapping Behavior and Hydrodynamic Drag. The finite element method (COMSOL Multiphysics 5.2a) is used to calculate the optical response of MM particles. A square cuboid-shaped particle is surrounded by a spherical region of uniform medium (water, n = 1.33), which is terminated by a perfectly matched layer shell. The scattering of the particle is calculated under background illumination by a tightly focused Gaussian beam that is linearly polarized along the x-axis and is described by the diffraction integral of Richards and Wolf.[59,60] Parameters used for the description of the focused beam, *e.g.*, the vacuum wavelength of 1064 nm, the NA of 1.2, and the aperture filling ratio of 1.7, are as in our experimental setup[23] and are also used to calculate the theoretical beam power. The optical forces and torques are retrieved by integrating the Maxwell stress tensor on the surface of a virtual sphere enclosing the MM nanocuboid.[61] These are used to extract the linear and angular trapping stiffness values, which are then normalized by the theoretically calculated input beam power.

For modeling the inner structure of an MM nanocuboid, we use an equivalent single-layer structure with effective optical constants predicted by EMT to calculate the optical trapping maps (Figure 2) rather than the actual multilayer structure, in order to reduce the calculation time. This approach has been validated by calculating the trapping forces and torques from both structures and showing that the resulting force and torque curves have only negligible differences

https://dx.doi.org/10.1021/acsnano.0c04233
ACS Nano 2020, 14, 14895−14906

(Figure S2). This comparison also confirms that EMT is a sufficiently precise description of our subwavelength multilayer structures at the operating wavelength of 1064 nm.

The viscous drag coefficients are also calculated by FEM (computational fluid dynamics module of COMSOL). The surrounding medium (water) is set to flow translationally (rotationally), inducing viscous drag force (torque) on the MM nanocuboid located at the center of the calculation domain. Solving the Navier–Stokes equations yields force and torque as a function of the speed of the medium flow, from which the linear (angular) drag coefficients are extracted.

These FEM models were initially validated in our previous report[23] to model rutile TiO_2 cylinders and only altered for the current work to use a square-cuboid instead of a cylinder as the particle geometry.

Sacrificial Layer-Based Top-Down Fabrication of MM Particles. The MM particles are fabricated in a top-down process (Figure S8a) that is adapted from our previous work.[22,23] First, a four-inch silicon (Si) wafer is cleaned with fuming (99.5%) HNO_3 (10 min), followed by thoroughly washing with DI water and spin-drying (Figure S8a, step 1). Next, a 100 nm thick sacrificial chromium (Cr) layer is deposited on the Si wafer by electron-beam evaporation (FC-2000, Temescal) with a deposition rate of 0.5 Å/s at a chamber pressure of $\sim 3 \times 10^{-7}$ Torr (Figure S8a, step 2). This slow deposition ensures a high-quality Cr coating with low surface roughness. Then, the Nb_2O_5/SiO_2 multilayer is deposited using plasma-assisted reactive magnetron sputtering (HELIOS, Bühler)[52] (Figure S8a, step 3), yielding highly reproducible refractive indices (Figure S9), while the layer thicknesses are controlled to ~1 nm precision with the aid of *in situ* optical monitoring[62] (Figure S9). The multilayer stack is designed to be symmetric by starting and finishing with SiO_2 layers of the same thickness. The detailed design of multilayer composition is described in Table S1.

The square-cuboid MM particles are shaped by lithography and etching with a Cr hard mask. First, the substrate is machine-diced to 1 cm × 1 cm chips, which are then cleaned with HNO_3 and DI water, as in the Si wafer preparation step. The samples are further cleaned in an ultrasonic bath with acetone and isopropyl alcohol (IPA), 5 min each, then spin-dried. A layer of ~250 nm thick positive-tone electron-beam resist (AR-P 6200.9, Allresist) is spin-coated (Figure S8a, step 4) and patterned by electron-beam lithography (EBPG 5000+, Vistec; patterning resolution of ~10 nm) with an exposure dose of 240 $\mu C/cm^2$ (Figure S8a, step 5). The particles are patterned in a hexagonal array (Figure S8b), with a gap size of 1 μm between adjacent particles. The development of the patterned resist layer is performed in an ultrasonic bath by sequential dipping in pentyl acetate (2 min), a 1:1 mixture of methyl isobutyl ketone and IPA (1 min), and IPA (1 min), then spin-dried. A hard etch mask layer (~70 nm thick Cr) is deposited by argon (Ar)-plasma sputtering (AC450, Alliance Concept), with a radio frequency (RF) power of 100 W, Ar supply of 20 sccm, and chamber pressure of 100 μbar (Figure S8a, step 6). These sputtering conditions are optimized for conformal deposition of Cr, allowing the enhanced etch mask shape, which results in more vertical sidewalls of particles after etching.[23] For lift-off, adhesive tape (Kapton) is initially used to remove most of the top Cr layer, and then the remaining resist layer is removed by dipping the sample in PRS-3000 (J.T. Baker) resist stripper at 80 °C for 30 min (Figure S8a, step 7). After rinsing the sample thoroughly with DI water and spin-drying, a reactive ion etcher (RIE; Fluor Z401S, Leybold Heraeus) is used to etch the multilayer vertically (Figure S8a, step 8). This dry etching uses a mixture of CHF_3 (50 sccm) and O_2 (3 sccm),[22] at a chamber pressure and RF power of 50 μbar and 200 W, respectively, resulting in an average multilayer etch rate of ~50 nm/min. To ensure the complete removal of the multilayer film within the unmasked region, ~15 s of additional etching is done after observing the endpoint by laser interferometry (LEM, HORIBA Scientific). In the same RIE machine, Ar-plasma sputter cleaning (20 sccm Ar flow, 10 μbar chamber pressure, and 100 W RF power) is performed for 5 min to remove an oxidized Cr layer from the surface of the hard mask and the sacrificial layer, which was probably induced during the previous dry etching step. This additional step enhances the result of wet etching for removal of remaining Cr layers in a later step, as oxidized Cr is less soluble in Cr etchant solution.

To retrieve the particles, the chips are manually cleaved into quarters, as the resulting smaller chips (approximately 5 mm × 5 mm each) can be inserted into a 2 mL volume plastic tube in a later step. Each chip is soaked in a Cr etchant solution (bright yellow; TechniEtch Cr01, MicroChemicals) for 10 min, where the top Cr mask and bottom sacrificial Cr layer are both dissolved (Figure S8a, step 9). Then, the chip is gently immersed in ample DI water for 30 s for the initial washing of Cr etchant droplets (the color of DI water turns light yellow after washing) (Figure S8a, step 10), followed by a second immersion in another beaker of DI water for 1 min without any agitation, which completely removes all etchant from its surface (after the second washing, the DI water remains as transparent as fresh water) (Figure S8a, step 11). Until this second immersion in DI water, most MM particles remain on the surface. However, they are visibly released from the surface when the chip is very slowly taken out of the second beaker of DI water and passed through the water–air interface while keeping its surface facing upward. The chip and the water droplet on its surface, which contains many released particles, are then jointly transferred into a 2 mL volume plastic tube containing 200 μL of fresh DI water, which is vortexed for 30 s (Figure S8a, step 12). The chip, whose surface is only clean Si after vortexing, is removed from the tube. The remaining particle solution is expected to have a concentration of $\sim 2 \times 10^4$ particles per μL, estimated from the solution volume, chip size, and pitch of the particle array (Figure S8b). As the particles are directly dispersible into water, the fraction of particles actually collected is much higher than in a previous top-down protocol for single-crystal substrates of quartz SiO_2 and rutile TiO_2, where a sacrificial layer cannot be included and particles could be lost or destroyed during their collection with a sharp blade and a pipette tip.[16,22] By SEM inspection of the randomly dispersed MM particles on a Si substrate, the complete removal of both the top Cr mask layer and the bottom Cr sacrificial layer has been observed (Figure S8c). This observation is further confirmed by the stable 3D optical trapping and highly homogeneous trapping parameters of MM particles, as 3D-trapping would become impossible or trapping performance would be inhomogeneous due to the high scattering force if any Cr layer remained on the MM particle surface. Although the MM particle fabrication is demonstrated with rather small samples here, our method is not limited to the shown chip sizes and can be scaled up.

Measurements of Linear and Angular Optical Trapping Properties. The optical trapping experiments are conducted in our custom-built optical torque wrench setup. The setup schematic and configuration are shown in Figure S11, and more details can be found in ref 23. For the sample chamber, we use a custom-made flow cell assembled with two borosilicate glass coverslips (No. 1.5H, Marienfeld) separated by a single-layer Parafilm spacer of ~100 μm thickness. The flow cell channel is completely filled with the MM particle solution without any air bubbles, and both the input and the output of the channel are sealed with vacuum grease (18405, Sigma-Aldrich). For all measurements, the MM particle solution is diluted until the concentration is low enough to have small probability of collision with other particles during measurements. It is notable that the laser beam power delivered at the focal plane inside the sample chamber is precisely calibrated[23] and used to normalize the measured trapping stiffness values.

We measured 10 different MM particle batches (A3–5, B3–5, and C3–6), and 3–7 particles were recorded from each batch (Figure S12, Table S2). For measurement and analysis of linear and angular trapping properties, we used our previously developed methods.[23] Notably, the frequency sweep method[23] is used in the torque–speed curve measurements (Figure 4).

ASSOCIATED CONTENT

Supporting Information

The Supporting Information is available free of charge at https://pubs.acs.org/doi/10.1021/acsnano.0c04233.

https://dx.doi.org/10.1021/acsnano.0c04233
ACS Nano 2020, 14, 14895–14906

Additional figures and tables (PDF)

AUTHOR INFORMATION

Corresponding Authors

Nynke H. Dekker − *Department of Bionanoscience, Kavli Institute of Nanoscience, Delft University of Technology, 2629 HZ Delft, The Netherlands*; Email: n.h.dekker@tudelft.nl

Aurèle J. L. Adam − *Optics Research Group, Department of Imaging Physics, Delft University of Technology, 2628 CJ Delft, The Netherlands*; Email: a.j.l.adam@tudelft.nl

Authors

Ying Tang − *Optics Research Group, Department of Imaging Physics, Delft University of Technology, 2628 CJ Delft, The Netherlands*

Seungkyu Ha − *Department of Bionanoscience, Kavli Institute of Nanoscience, Delft University of Technology, 2629 HZ Delft, The Netherlands*; orcid.org/0000-0002-0564-0790

Thomas Begou − *Aix Marseille Univ, CNRS, Centrale Marseille, Institut Fresnel, 13013 Marseille, France*

Julien Lumeau − *Aix Marseille Univ, CNRS, Centrale Marseille, Institut Fresnel, 13013 Marseille, France*

H. Paul Urbach − *Optics Research Group, Department of Imaging Physics, Delft University of Technology, 2628 CJ Delft, The Netherlands*

Complete contact information is available at: https://pubs.acs.org/10.1021/acsnano.0c04233

Author Contributions

[§]Y. Tang and S. Ha equally contributed to this work.

Author Contributions

Y.T., S.H., N.H.D., and A.J.L.A. designed the research. A.J.L.A. and N.H.D. directed the research. Y.T. conducted theoretical calculations, developed FEM numerical models, and fabricated MM particles from multilayer structures. S.H. advised on the fabrication, conducted experimental measurements, and analyzed the experimental data. T.B. and J.L. deposited the multilayer structures. Y.T., S.H., H.P.U., N.H.D., and A.J.L.A. discussed the data. Y.T., S.H., N.H.D., and A.J.L.A. wrote the manuscript.

Notes

The authors declare no competing financial interest.

ACKNOWLEDGMENTS

We thank Joseph Braat for advice on optical modeling; Daniel Tam for advice on developing numerical models for drag coefficient calculation; Marc Zuiddam, Charles de Boer, Marco van der Krogt, Hozanna Miro, Arnold van Run, Anja van Langen-Suurling, Wiel Evers, Majid Ahmadi, and Iman Esmaeil Zadeh for technical advice on nanofabrication; Margreet Docter, Roland Dries, and Jacob Kerssemakers for technical advice on the OTW setup; Dimitri de Roos for the production of custom-made mechanical parts for the OTW setup; Theo van Laar and Sacha Khaiboulov for help with laboratory infrastructure; and Kaley McCluskey, Belen Solano, and Jacob Hoogenboom for reviewing the manuscript. This work is supported by the Faculty of Applied Sciences at Delft University of Technology (scienceDATE grant 2017; to Y.T. and S.H.); by funding provided by the China Scholarship Council under grant number 201306160089 (to Y.T.); by NanoNextNL, a micro- and nanotechnology consortium of the Government of The Netherlands and 130 partners (to N.H.D.); by the Department of Bionanoscience at Delft University of Technology (to N.H.D.); by the Foundation for Fundamental Research on Matter (FOM), part of The Netherlands Organisation for Scientific Research (NWO) (to N.H.D); and by the European Research Council (ERC) Consolidator Grant under grant number 312221 (DynGenome; to N.H.D.).

REFERENCES

(1) Gao, D.; Ding, W.; Nieto-Vesperinas, M.; Ding, X.; Rahman, M.; Zhang, T.; Lim, C.; Qiu, C.-W. Optical Manipulation from the Microscale to the Nanoscale: Fundamentals, Advances and Prospects. *Light: Sci. Appl.* **2017**, *6*, e17039.

(2) Polimeno, P.; Magazzù, A.; Iatì, M. A.; Patti, F.; Saija, R.; Boschi, C. D. E.; Donato, M. G.; Gucciardi, P. G.; Jones, P. H.; Volpe, G.; Maragò, O. M. Optical Tweezers and Their Applications. *J. Quant. Spectrosc. Radiat. Transfer* **2018**, *218*, 131−150.

(3) Ding, W.; Zhu, T.; Zhou, L.-M.; Qiu, C.-W. Photonic Tractor Beams: A Review. *Advanced Photonics* **2019**, *1*, 024001.

(4) Capitanio, M.; Pavone, F. S. Interrogating Biology with Force: Single Molecule High-Resolution Measurements with Optical Tweezers. *Biophys. J.* **2013**, *105*, 1293−1303.

(5) Forth, S.; Sheinin, M. Y.; Inman, J.; Wang, M. D. Torque Measurement at the Single-Molecule Level. *Annu. Rev. Biophys.* **2013**, *42*, 583−604.

(6) Lipfert, J.; van Oene, M. M.; Lee, M.; Pedaci, F.; Dekker, N. H. Torque Spectroscopy for the Study of Rotary Motion in Biological Systems. *Chem. Rev.* **2015**, *115*, 1449−1474.

(7) van Oene, M. M.; Ha, S.; Jager, T.; Lee, M.; Pedaci, F.; Lipfert, J.; Dekker, N. H. Quantifying the Precision of Single-Molecule Torque and Twist Measurements Using Allan Variance. *Biophys. J.* **2018**, *114*, 1970−1979.

(8) Arita, Y.; Mazilu, M.; Dholakia, K. Laser-Induced Rotation and Cooling of a Trapped Microgyroscope in Vacuum. *Nat. Commun.* **2013**, *4*, 2374.

(9) Ahn, J.; Xu, Z.; Bang, J.; Deng, Y.-H.; Hoang, T. M.; Han, Q.; Ma, R.-M.; Li, T. Optically Levitated Nanodumbbell Torsion Balance and GHz Nanomechanical Rotor. *Phys. Rev. Lett.* **2018**, *121*, 033603.

(10) Nan, F.; Yan, Z. Silver-Nanowire-Based Interferometric Optical Tweezers for Enhanced Optical Trapping and Binding of Nanoparticles. *Adv. Funct. Mater.* **2019**, *29*, 1808258.

(11) Williams, I.; Oßuz, E. C.; Speck, T.; Bartlett, P.; Löwen, H.; Royall, C. P. Transmission of Torque at the Nanoscale. *Nat. Phys.* **2016**, *12*, 98−103.

(12) Shao, L.; Yang, Z. J.; Andrén, D.; Johansson, P.; Käll, M. Gold Nanorod Rotary Motors Driven by Resonant Light Scattering. *ACS Nano* **2015**, *9*, 12542−12551.

(13) Shen, Z.; Su, L.; Yuan, X. C.; Shen, Y. C. Trapping and Rotating of a Metallic Particle Trimer with Optical Vortex. *Appl. Phys. Lett.* **2016**, *109*, 241901.

(14) Deufel, C.; Forth, S.; Simmons, C. R.; Dejgosha, S.; Wang, M. D. Nanofabricated Quartz Cylinders for Angular Trapping: DNA Supercoiling Torque Detection. *Nat. Methods* **2007**, *4*, 223−225.

(15) Gutiérrez-Medina, B.; Andreasson, J. O. L.; Greenleaf, W. J.; LaPorta, A.; Block, S. M. An Optical Apparatus for Rotation and Trapping. In *Methods in Enzymology*; Walter, N. G., Ed.; Academic Press: San Diego, CA, 2010; Vol. *475*, pp 377−404.

(16) Huang, Z.; Pedaci, F.; van Oene, M.; Wiggin, M. J.; Dekker, N. H. Electron Beam Fabrication of Birefringent Microcylinders. *ACS Nano* **2011**, *5*, 1418−1427.

(17) Li, P.-C.; Chang, J.-C.; La Porta, A.; Yu, E. T. Fabrication of Birefringent Nanocylinders for Single-Molecule Force and Torque Measurement. *Nanotechnology* **2014**, *25*, 235304.

(18) Santybayeva, Z.; Meghit, A.; Desgarceaux, R.; Teissier, R.; Pichot, F.; de Marin, C.; Charlot, B.; Pedaci, F. Fabrication of Quartz Microcylinders by Laser Interference Lithography for Angular Optical Tweezers. *J. Micro/Nanolithogr., MEMS, MOEMS* **2016**, *15*, 034507.

(19) Friese, M. E. J.; Nieminen, T. A.; Heckenberg, N. R.; Rubinsztein-Dunlop, H. Optical Alignment and Spinning of Laser-Trapped Microscopic Particles. *Nature* **1998**, *394*, 348−350.
(20) Arita, Y.; Richards, J. M.; Mazilu, M.; Spalding, G. C.; Spesyvtseva, S. E. S.; Craig, D.; Dholakia, K. Rotational Dynamics and Heating of Trapped Nanovaterite Particles. *ACS Nano* **2016**, *10*, 11505−11510.
(21) Ramaiya, A.; Roy, B.; Bugiel, M.; Schäffer, E. Kinesin Rotates Unidirectionally and Generates Torque While Walking on Microtubules. *Proc. Natl. Acad. Sci. U. S. A.* **2017**, *114*, 10894.
(22) Ha, S.; Janissen, R.; Ussembayev, Y. Y.; van Oene, M. M.; Solano, B.; Dekker, N. H. Tunable Top-Down Fabrication and Functional Surface Coating of Single-Crystal Titanium Dioxide Nanostructures and Nanoparticles. *Nanoscale* **2016**, *8*, 10739−10748.
(23) Ha, S.; Tang, Y.; van Oene, M. M.; Janissen, R.; Dries, R. M.; Solano, B.; Adam, A. J. L.; Dekker, N. H. Single-Crystal Rutile TiO_2 Nanocylinders Are Highly Effective Transducers of Optical Force and Torque. *ACS Photonics* **2019**, *6*, 1255−1265.
(24) Singer, W.; Nieminen, T. A.; Gibson, U. J.; Heckenberg, N. R.; Rubinsztein-Dunlop, H. Orientation of Optically Trapped Nonspherical Birefringent Particles. *Phys. Rev. E* **2006**, *73*, 021911.
(25) Bareil, P. B.; Sheng, Y. Angular and Position Stability of a Nanorod Trapped in an Optical Tweezers. *Opt. Express* **2010**, *18*, 26388−26398.
(26) Ghosh, G. Dispersion-Equation Coefficients for the Refractive Index and Birefringence of Calcite and Quartz Crystals. *Opt. Commun.* **1999**, *163*, 95−102.
(27) Christy, A. G. A Review of the Structures of Vaterite: The Impossible, the Possible, and the Likely. *Cryst. Growth Des.* **2017**, *17*, 3567−3578.
(28) DeVore, J. R. Refractive Indices of Rutile and Sphalerite. *J. Opt. Soc. Am.* **1951**, *41*, 416−419.
(29) Malitson, I. H. Interspecimen Comparison of the Refractive Index of Fused Silica. *J. Opt. Soc. Am.* **1965**, *55*, 1205−1209.
(30) Sultanova, N.; Kasarova, S.; Nikolov, I. Dispersion Properties of Optical Polymers. *Acta Phys. Pol., A* **2009**, *116*, 585−587.
(31) Stallinga, S. Optical Trapping at Low Numerical Aperture. *J. Eur. Opt. Soc.* **2011**, *6*, 11027.
(32) Hwu, E. E.-T.; Boisen, A. Hacking CD/DVD/Blu-Ray for Biosensing. *ACS Sensors* **2018**, *3*, 1222−1232.
(33) Higurashi, E.; Sawada, R.; Ito, T. Optically Induced Rotation of a Trapped Micro-Object About an Axis Perpendicular to the Laser Beam Axis. *Appl. Phys. Lett.* **1998**, *72*, 2951−2953.
(34) Neale, S. L.; MacDonald, M. P.; Dholakia, K.; Krauss, T. F. All-Optical Control of Microfluidic Components Using Form Birefringence. *Nat. Mater.* **2005**, *4*, 530−533.
(35) Friedrich, L.; Rohrbach, A. Surface Imaging beyond the Diffraction Limit with Optically Trapped Spheres. *Nat. Nanotechnol.* **2015**, *10*, 1064−1069.
(36) Padilla, W. J.; Basov, D. N.; Smith, D. R. Negative Refractive Index Metamaterials. *Mater. Today* **2006**, *9*, 28−35.
(37) Choi, M.; Lee, S. H.; Kim, Y.; Kang, S. B.; Shin, J.; Kwak, M. H.; Kang, K.-Y.; Lee, Y.-H.; Park, N.; Min, B. A Terahertz Metamaterial with Unnaturally High Refractive Index. *Nature* **2011**, *470*, 369−373.
(38) Min, L.; Huang, L.; Sun, R.; Xi, M.; Li, Z. Dual Metamaterial with Large Birefringence. *IEEE Photonics J.* **2015**, *7*, 4600608.
(39) Guo, Y.; Newman, W.; Cortes, C. L.; Jacob, Z. Applications of Hyperbolic Metamaterial Substrates. *Adv. OptoElectron.* **2012**, *2012*, 452502.
(40) Jahani, S.; Jacob, Z. All-Dielectric Metamaterials. *Nat. Nanotechnol.* **2016**, *11*, 23−36.
(41) Lang, S.; Lee, H.; Petrov, A. Y.; Störmer, M.; Ritter, M.; Eich, M. Gold-Silicon Metamaterial with Hyperbolic Transition in near Infrared. *Appl. Phys. Lett.* **2013**, *103*, 021905.
(42) Kruk, S. S.; Wong, Z. J.; Pshenay-Severin, E.; O'brien, K.; Neshev, D. N.; Kivshar, Y. S.; Zhang, X. Magnetic Hyperbolic Optical Metamaterials. *Nat. Commun.* **2016**, *7*, 11329.
(43) Kelly, P.; Liu, M.; Kuznetsova, L. Designing Optical Metamaterial with Hyperbolic Dispersion Based on an Al:ZnO/ZnO Nano-Layered Structure Using the Atomic Layer Deposition Technique. *Appl. Opt.* **2016**, *55*, 2993−2997.
(44) Hernandez, C. J.; Mason, T. G. Colloidal Alphabet Soup: Monodisperse Dispersions of Shape-Designed Lithoparticles. *J. Phys. Chem. C* **2007**, *111*, 4477−4480.
(45) Clericò, V.; Masini, L.; Boni, A.; Meucci, S.; Cecchini, M.; Recchia, F. A.; Tredicucci, A.; Bifone, A. Water-Dispersible Three-Dimensional LC-Nanoresonators. *PLoS One* **2014**, *9*, e105474.
(46) Badman, R. P.; Ye, F.; Caravan, W.; Wang, M. D. High Trap Stiffness Microcylinders for Nanophotonic Trapping. *ACS Appl. Mater. Interfaces* **2019**, *11*, 25074−25080.
(47) Cai, W.; Shalaev, V. *Optical Metamaterials*; Springer: New York, NY, 2010.
(48) El Gawhary, O.; Dheur, M.; Pereira, S.; Braat, J. Extension of the Classical Fabry-Perot Formula to 1D Multilayered Structures. *Appl. Phys. B: Lasers Opt.* **2013**, *111*, 637−645.
(49) Sperling, R. A.; Parak, W. J. Surface Modification, Functionalization and Bioconjugation of Colloidal Inorganic Nanoparticles. *Philos. Trans. R. Soc., A* **2010**, *368*, 1333−1383.
(50) Pujari, S. P.; Scheres, L.; Marcelis, A. T. M.; Zuilhof, H. Covalent Surface Modification of Oxide Surfaces. *Angew. Chem., Int. Ed.* **2014**, *53*, 6322−6356.
(51) Reimhult, E.; Höök, F. Design of Surface Modifications for Nanoscale Sensor Applications. *Sensors* **2015**, *15*, 1635−1675.
(52) Lumeau, J.; Lemarchand, F.; Begou, T.; Arhilger, D.; Hagedorn, H. Angularly Tunable Bandpass Filter: Design, Fabrication, and Characterization. *Opt. Lett.* **2019**, *44*, 1829−1832.
(53) Madadi, E.; Samadi, A.; Cheraghian, M.; Reihani, S. N. S. Polarization-Induced Stiffness Asymmetry of Optical Tweezers. *Opt. Lett.* **2012**, *37*, 3519−3521.
(54) Santybayeva, Z.; Pedaci, F. Optical Torque Wrench Design and Calibration. In *Optical Tweezers: Methods and Protocols*; Gennerich, A., Ed.; Springer New York: New York, NY, 2017; pp 157−181.
(55) Muradoglu, M.; Ng, T. W. Optical Trapping Map of Dielectric Spheres. *Appl. Opt.* **2013**, *52*, 3500−3509.
(56) Reihani, S. N. S.; Mir, S. A.; Richardson, A. C.; Oddershede, L. B. Significant Improvement of Optical Traps by Tuning Standard Water Immersion Objectives. *J. Opt.* **2011**, *13*, 105301.
(57) Rohrbach, A.; Stelzer, E. H. K. Trapping Forces, Force Constants, and Potential Depths for Dielectric Spheres in the Presence of Spherical Aberrations. *Appl. Opt.* **2002**, *41*, 2494−2507.
(58) Nord, A. L.; Gachon, E.; Perez-Carrasco, R.; Nirody, J. A.; Barducci, A.; Berry, R. M.; Pedaci, F. Catch Bond Drives Stator Mechanosensitivity in the Bacterial Flagellar Motor. *Proc. Natl. Acad. Sci. U. S. A.* **2017**, *114*, 12952−12957.
(59) Wolf, E.; Gabor, D. Electromagnetic Diffraction in Optical Systems - I. An Integral Representation of the Image Field. *Proc. R. Soc. London A* **1959**, *253*, 349−357.
(60) Richards, B.; Wolf, E.; Gabor, D. Electromagnetic Diffraction in Optical Systems, II. Structure of the Image Field in an Aplanatic System. *Proc. R. Soc. London A* **1959**, *253*, 358−379.
(61) Chen, J.; Ng, J.; Lin, Z.; Chan, C. T. Optical Pulling Force. *Nat. Photonics* **2011**, *5*, 531−534.
(62) Macleod, H. A. *Thin Film Optical Filters*; Institute of Physics Publishing: Bristol, 2001.

NOTE ADDED AFTER ASAP PUBLICATION

This article was published ASAP on November 10, 2020, with incorrect Supporting Information. The corrected version was reposted on November 11, 2020.

https://dx.doi.org/10.1021/acsnano.0c04233
ACS Nano 2020, 14, 14895−14906